Analytical and numerical calculations of the magnetic force microscopy response: A comparison

R. Engel-Herbert, D. M. Schaadt, and T. Hesjedal[a)]
Paul-Drude-Institut für Festkörperelektronik, Hausvogteiplatz 5-7, D-10117 Berlin, Germany

(Received 28 November 2005; accepted 3 March 2006; published online 9 June 2006)

We investigate the domain structure of submicrometer sized ferromagnetic stripes exhibiting in-plane and out-of-plane magnetized areas with magnetic force microscopy (MFM). Two simulation approaches are used to calculate the observed MFM response. The first relies on an analytical solution for the stray field of a bar magnet and the subsequent modeling of the sample as an arrangement of bar magnets. The MFM response is calculated for a realistic tip shape incorporating a distribution of magnetic dipoles. The second, numerical approach is based on a discretization scheme, breaking the tip-sample problem up into cells and then calculating the energy of the magnetic tip-sample interaction. The MFM responses obtained for the ferromagnetic stripe structure are compared. A discussion of the advantages and limitations of the two methods is given in terms of precision, computing time, and flexibility. The numerical method offers shorter computing times and greater flexibility, opening the door for realistic three-dimensional MFM response simulations. The advantage of the analytical method is the investigation of small structures, as its precision is higher for the comparable computational effort. © *2006 American Institute of Physics*. [DOI: 10.1063/1.2202242]

I. INTRODUCTION

Since its introduction in 1987,[1,2] magnetic force microscopy (MFM) has proven a very useful micromagnetic imaging technique for basic and applied research, reaching from magnetic domain structures to magnetic storage media and read heads.[3,4] MFM is based on noncontact force microscopy in combination with magnetically coated tips and allows for the mapping of a sample's stray field with submicron lateral resolution. The MFM response, i.e., the response due to the magnetic interaction between tip and sample, enables in many cases for a qualitative characterization of the micromagnetic properties of a sample, such as the hard[5] or soft[6] magnetic properties, or even the determination of the nature of domain walls as Bloch-or Néel-like.[7,8]

The quantitative interpretation of MFM results, on the other hand, is a challenging task. The magnetic interaction force between the tip and the sample, $\mathbf{F}=-\nabla E_{t-s}$, is determined by the convolution of the tip magnetization $\mathbf{M}_{\text{tip}}$ with the sample stray field $\mathbf{H}_s$: $E_{t-s} \sim \int_{\text{tip}} \mathbf{M}_{\text{tip}} \mathbf{H}_s$. In case of mutual nondisturbance of tip and sample magnetization, the convolution of the sample magnetization $\mathbf{M}_s$ and tip stray field $\mathbf{H}_{\text{tip}}$ yields the same result and, by knowing the precise tip stray field, one can, in principle, determine the sample magnetization $\mathbf{M}_s$. The first problem arises as different magnetization patterns will lead to the same stray field at a certain distance above the sample.[9] The second problem is related to the magnetic probe in MFM. As the measured response is governed by the tip properties which are usually not known in detail,[10] some effort has been dedicated to develop suited calibration standards for MFM tips such as current strips[11] and rings.[12] A few attempts have been made to measure the magnetic stray field of the tip by electron holography,[13] Lorentz microscopy,[14,15] and micro-Hall-probe measurements.[16] Also, the magnetization distribution of the tip has been calculated, assuming the tip as a two-dimensional triangular structure[17] and based on a three-dimensional model.[18] Nevertheless, it has to be noted that the calibration of the tip is laborious to obtain and, furthermore, the tip properties are difficult to maintain in the experiment. Beyond this effort, MFM tips are known to influence the magnetic structure of the sample under investigation, which was a basic assumption for the extraction of the sample magnetization above.[7,19]

The simulation of the MFM contrast[20] has been performed using different approaches, which we are not going to review in detail. For reviews see, e.g., Refs. 21 and 19. Due to the complexity of the problem, practical MFM simulations are based on a number of approximations mainly concerning a realistic tip magnetization. Common approaches are the point dipole model,[22] the ellipsoidal dipole model,[23] and the magnetic charge model.[14] This way, the MFM response in complex stray fields above current-carrying rings was calculated and measured.[24] More advanced tip models involve a spherical apex and a conical taper,[25] a conically shaped tip,[26] a nonmagnetic truncated cone covered by a thin magnetic layer,[27] and a discretized probe,[17] which are applied to samples with rather simple and well-known stray fields. For calculating the MFM response and resolution of samples with periodic magnetization features, such as recording media, a Fourier transform approach was introduced for obtaining the sample stray field.[28,29] For more complex situations, i.e., for nonperiodic magnetizations where every magnetic sample charge has to be Fourier transformed and for films with a magnetization distribution in depth, the method loses its advantages. The problem of the tip influence

[a)]Present address: Electrical and Computer Engineering Department, University of Waterloo, Waterloo, Ontario NZL 3G1, Canada; electronic mail: hesjedal@pdi-berlin.de

on the sample magnetization has been addressed in the framework of micromagnetism, where the tip was treated as an effective monopole.[30] The proper approach, however, relies on time-consuming iterative energy minimization techniques. The magnetization state with the lowest energy, taking into account exchange, anisotropy, and magnetostatic energies, represents the equilibrium magnetization state of the MFM tip[31] and the sample. An impressive example was the calculation of the disturbance of the domain wall of a FeNi film in the presence of a Fe tip.[32]

The progress in magnetic nanostructures, e.g., for spintronic applications, requires a quantitative modeling of the MFM response based on more realistic assumptions. Based on such simulations, the influence of the scan parameters (scan speed, tip-sample distance) and a realistic tip on the MFM contrast can be studied and, finally, the in-plane and out-of-plane magnetization distributions can be determined. For our studies, we chose a material system which exhibits an ordered array of ferromagnetic/nonmagnetic stripes on a submicron scale as a result of self-organization. Each ferromagnetic (FM) stripe shows a sequence of oppositely magnetized domains giving rise to a large out-of-plane component of the stray field at their ends, separated by 180° Bloch walls.

The structure of this paper is as follows. We take two approaches for the calculation of the MFM response. We view the FM stripes as a sequence of oppositely magnetized bar magnets in plane, separated by narrow bar magnets oriented out of plane mimicking the Bloch walls. In a first approach, the stray field of the bar magnet is obtained from an analytical solution.[33] The MFM response is then calculated as a convolution of the sample stray field with the magnetization distribution of the tip. The tip is modeled in an extended dipole model, i.e., a distribution of dipoles in the tip volume. The second approach is a three-dimensional calculation of the magnetization state of the tip-sample problem, including realistic magnetization distributions for tip and sample. Based on the model system MnAs-on-GaAs(001), we compare the simulation of the MFM contrast using both approaches and discuss the computational effort, precision, and the limitations.

II. MODEL SYSTEM: MnAs-on-GaAs(001)

So far, a quantitative modeling of the MFM contrast has been reached for a number of systems,[14,30] such as current-carrying strips[11] and magneto-optic samples.[34] For our investigations, we chose a material system that exhibits a self-organized, periodic structure of ferromagnetic stripes. Their width can be adjusted in a range of ≈100–1000 nm via the temperature. The well-characterized magnetic domain pattern on a stripe resembles a sequence of antiparallelly magnetized bar magnets. The magnetization remains in plane and oriented along the easy axis of magnetization. The segments are separated by ≈10 nm wide 180° Bloch-type domain walls. Thus, this material system exhibits a versatile playground for micromagnetic measurements and simulations as the geometrical parameters of the nanomagnets, exhibiting in-plane and out-of-plane magnetization components, can be easily adjusted.

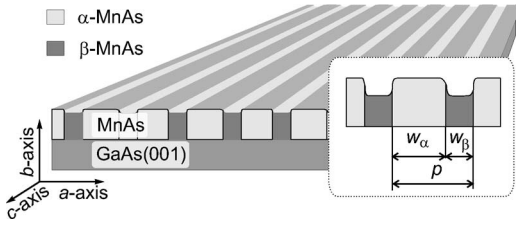

FIG. 1. Self-organized magnetic nanostructure. MnAs-on-GaAs(001) exhibits an alternating array of ferromagnetic α-MnAs and nonmagnetic β-MnAs stripes elongated along the c-axis direction. The stripe widths $w_{\alpha/\beta}$ can be tuned by the temperature, while the stripe period p is a function of film thickness.

A. Structural and magnetic properties

MnAs-on-GaAs(001) is a quite unique hybrid semiconductor-ferromagnetic materials system that generated some interest as spin injection[35] and magnetologic[36] applications have been demonstrated. MnAs can be grown epitaxially on GaAs(001) (Refs. 37 and 38) and other substrates[39] and shows a Curie temperature (in the bulk) of ≈40 °C.[40–42] The epitaxial orientation of MnAs on GaAs(001) is MnAs($\bar{1}$100)‖GaAs(001) and MnAs[0001] (c axis) ‖GaAs[1$\bar{1}$0].[38] The investigated films have a nominal thickness of 180 nm. The material system exhibits two structurally and magnetically distinct phases coexisting from 10 to 40 °C as a result of the involved strain[43,44] in the course of the first order phase transition. The phase transformation from the hexagonal, ferromagnetic α phase to the orthorhombic, nonmagnetic β phase involves a discontinuous expansion of the lattice along the a axes (of bulk MnAs) by ≈1%, whereas the lattice parameter c remains nearly unchanged.[45] MnAs films, on the other hand, that can only expand along the growth direction, exhibiting a self-organized $\alpha-\beta$-stripe structure oriented along the MnAs[0001] (c-axis) direction as a result of the involved strain. Due to the lattice expansion in the growth direction, the $\alpha-\beta$-stripe structure is easily observable as a ridge-groove pattern. A sketch of the $\alpha-\beta$-stripe structure is shown in Fig. 1.

The topography and micromagnetic structure of MnAs films in the $\alpha-\beta$-stripe phase have been extensively studied as functions of temperature,[44,46] film thickness,[47] and magnetic field[48] using atomic force microscopy, MFM, and x-ray diffraction.[43] It has been found that the stripe period p scales linearly with the film thickness t (p=4.8t).[47] The width of the α and β stripes, w_α and w_β, on the other hand, is a function of the temperature.[44,46] The magnetic properties of the films were determined by using a superconducting quantum interference device (SQUID) magnetometer. Bulk MnAs exhibits an easy plane of magnetization perpendicular to the c axis (hard axis). For thin films, the easy plane separates due to the shape anisotropy into an easy axis along the MnAs[1$\bar{1}$20] direction (a axis) and an intermediate axis along the growth direction (b axis).

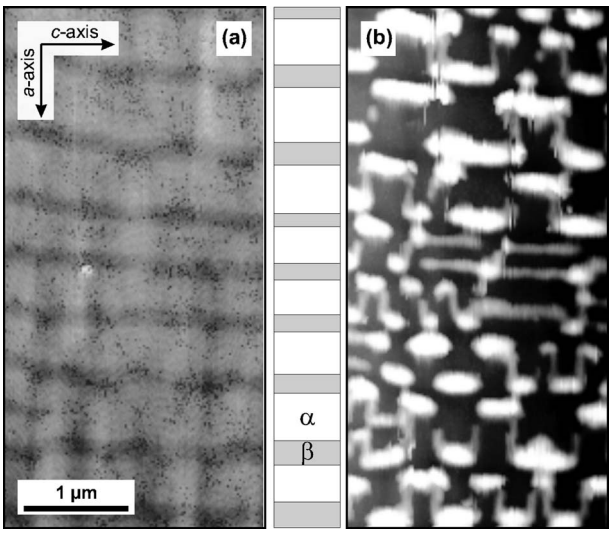

FIG. 2. (a) Representative topography and (b) MFM image of a MnAs film at room temperature. In the middle, the positions of the α- and β-MnAs stripes are indicated; the ferromagnetic α stripes extend in height.

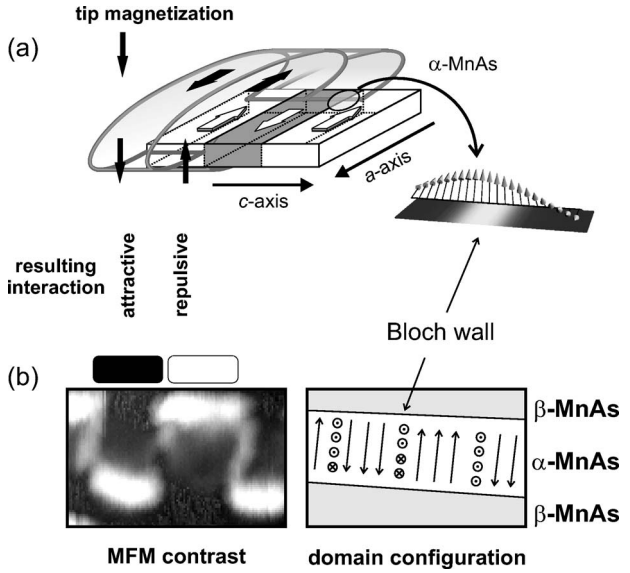

FIG. 3. (a) Micromagnetic domain structure and resulting stray field of a ferromagnetic α stripe. The commonly observed type (I) domains can be modeled as a sequence of oppositely magnetized bar magnets separated by a 180° Bloch wall (see right-hand side). An attractive (repulsive) magnetic interaction between the tip (magnetized along its axis) and the sample magnetization at the respective ends of the bar magnets results in dark (bright) MFM contrast. (b) Experimental MFM image (left) and corresponding magnetization distribution (right).

B. Micromagnetic properties

Figure 2 shows a typical MFM scan of a MnAs film at room temperature. The magnetic contrast of the α stripes is dominated by a meanderlike pattern extending along the stripes.[49] The positions of the α- and β-MnAs stripes, obtained from the height modulation in the topography image, are indicated on the right-hand side. A closer look on the magnetic structure [Fig. 3(b)] reveals alternating bright areas at both ends of the FM stripes (stretching along the *c*-axis direction). These areas are partially connected by narrower bright lines. The observed MFM contrast can be understood by assuming a sequence of alternatingly magnetized bar magnet-like domains (magnetization entirely along the easy *a* axis), separated by 180° Bloch walls pointing into and out of the sample plane [see Fig. 3(a)]. This assumption is justified as SQUID measurements reveal that the film has one easy magnetization direction along the width of the stripe.

Figure 3 explains the contrast mechanism resulting from the interaction of the tip magnetization with the stray field of the domains. The magnetic stray field of the bar magnetlike domains will either point up (out of the plane) or point down (back into the plane) at the end of a ferromagnetic stripe, as shown by the arrows in the top left sketch in Fig. 3(a). The MFM is sensitive to out-of-plane component of the stray field which interacts with the tip magnetization (along the tip axis, see downward pointing arrow). The interaction between the tip and the stray field of the sample depends on the relative orientation of these two vectors. The parallel (antiparallel) orientation of the two magnetization vectors results in an attractive (repulsive) interaction, giving a dark (bright) contrast as shown in Fig. 3(b). Besides this contribution to the contrast, narrower dark and bright lines are also seen between two oppositely oriented domains. This is due to 180° Bloch walls where the magnetization vector rotates through the surface normal direction (pointing out of or into the plane) to reverse its direction between two oppositely magnetized in-plane domains [see Fig. 3(a), right]. On the right of Fig. 3(b), the most likely domain configuration (including the orientation of the Bloch walls) is sketched that matches best the experimental image on the left. The differences between the orientational distribution of neighboring Bloch walls are not understood yet.

In the following sections, the MFM response originating from such a domain configuration will be derived based on an analytical (Sec. III) and a numerical model (Sec. IV) and finally compared in Sec. V.

III. MFM RESPONSE: ANALYTICAL SOLUTION

We start with a discussion of the MFM response based on an analytical expression for the stray field of a bar magnet. This way, the magnetic stray field of the MnAs film can be modeled by a superposition of in-plane magnetized bar magnets, separated by out-of-plane magnetized bar magnets representing the Bloch wall. For calculating the MFM response, a realistic tip model was used, assuming a distribution of dipoles in the magnetic tip coating. In order to investigate the influence of the accessible experimental parameters (tip-sample distance z_0, tip and sample magnetizations M_{tip} and M_s, and tip and sample geometry) on the MFM response we kept the simulation as simple as possible. In the model, we assume a static magnetic configuration thus excluding dynamic magnetization effects. Furthermore, we neglect a mutual disturbance of the magnetization distributions of tip and sample.

A. Theoretical consideration of the MFM response

The force density $\mathbf{f}$ acting on the MFM tip with magnetization $\mathbf{M}_{\mathrm{tip}}$ in the stray field of the sample $\mathbf{H}_s$ is given by $\mathbf{f}=\mu_0\cdot\nabla(\mathbf{M}_{\mathrm{tip}}\cdot\mathbf{H}_s)$ and simplifies in the case of mutual nondisturbance to

$$\mathbf{f} = \mu_0(\mathbf{M}_{\text{tip}} \cdot \nabla)\mathbf{H}_s. \quad (1)$$

MFM is based on dynamic force microscopy using a magnetically coated tip. The cantilever is excited to oscillate close to its resonance frequency with an amplitude A_d and at a frequency ω_d. The deflection of the cantilever motion, and hence the force gradient, is typically detected by an optical beam-bounce technique with a resolution <1 Å. The image is obtained by raster scanning the tip across the sample and recording the change in the cantilever oscillation due to the tip-sample interaction. The motion of the cantilever beam can be modeled as a one-dimensional damped, driven harmonic oscillator with quality factor Q, spring constant k, and effective mass m, exhibiting a resonant frequency $\omega_0 = \sqrt{k/m}$.[3] The free oscillation of the cantilever is perturbed in a force field. The tip-sample interaction can be treated as a spring in series with the cantilever. An attractive force, and thus a positive force gradient ($F' > 0$), will make the cantilever spring softer. The effective spring constant of the cantilever is as follows:

$$k_{\text{eff}} = k - F'. \quad (2)$$

The change in spring constant due to the force gradient causes a shift in the resonance frequency of the cantilever $\omega_r = \sqrt{(k-F')/m}$. In a linear approximation, the frequency shift can be written as

$$\Delta\omega \cong \frac{\omega_0 F'}{2k}. \quad (3)$$

In addition, the oscillation amplitude and the phase shift are linear functions of the force gradient and can also be utilized for MFM imaging.[50]

For the following discussion of the force gradient, only the normal component $\mathbf{F}_n$ of the total tip-sample interaction force is considered:

$$F_n'(\mathbf{r}) = \frac{d\mathbf{F}_n}{dn} = \mathbf{n} \cdot \nabla_{\mathbf{r}}[\mathbf{n} \cdot \mathbf{F}_{\text{tot}}(\mathbf{r})], \quad (4)$$

where $\mathbf{n}$ is collinear with the oscillation direction of the cantilever.[1,25]

The total magnetic interaction between sample and tip is given by the convolution of the magnetic field emanating from the sample $\mathbf{H}_s$ and the magnetization of the tip $\mathbf{M}_{\text{tip}}$, leading to a total force,

$$\mathbf{F}_{\text{tot}}(\mathbf{r}) = \mu_0 \int_{\text{tip}} (\mathbf{M}_{\text{tip}}(\mathbf{r}') \cdot \nabla_{\mathbf{r}})\mathbf{H}_s(\mathbf{r} - \mathbf{r}')d^3\mathbf{r}'. \quad (5)$$

By inserting Eq. (5) in Eq. (4), the force gradient can be written as

$$F_n'(\mathbf{r}) = \mathbf{n} \cdot \nabla_{\mathbf{r}} \left\{ \mathbf{n} \cdot \mu_0 \int_{\text{tip}} [\mathbf{M}_{\text{tip}}(\mathbf{r}') \cdot \nabla_{\mathbf{r}}]\mathbf{H}_s(\mathbf{r} - \mathbf{r}')d^3\mathbf{r}' \right\}. \quad (6)$$

A careful discussion of Eq. (6) is important for interpreting the simulations. For simplification, the normal vector is related to the surface of the sample as follows: $\mathbf{n} = \mathbf{e_z}$. Then, only the z component of the total force gradient contributes to the frequency shift. That simplifies Eq. (6) further, yielding

$$F_z'(\mathbf{r}) = \mu_0 \int_{\text{tip}} \left[M_{z,\text{tip}}(\mathbf{r}') \cdot \frac{\partial^2}{\partial z^2} H_z(\mathbf{r} - \mathbf{r}')d^3\mathbf{r}' \right]. \quad (7)$$

Our assumption that $\mathbf{n} = \mathbf{e_z}$, and thus $F' = \partial F_z / \partial z$, neglects the tilt of the cantilever that is usually present in an experimental geometry. As a result, the experimental MFM contrast is asymmetric with respect to the line of zero magnetic force. However, as this effect is rather small, it will be neglected in our discussion.[25]

B. Tip model

In general, the magnetic and geometrical properties of the tip are influencing the MFM response [see Eq. (5)]. Consequently, the tip shape as well as the magnetic coating have to be treated in a suitable model. We use a tip model where the real magnetic coating is represented by a distribution of dipoles. For simple sample stray fields, such as a single point dipole,[26,27] a direct integration over the tip is possible. For more complicated stray fields, e.g., the stray field of current-carrying lines,[11,51] parallel wires,[52–55] or rings,[12,24] the tip is approximated by a point dipole. In general, satisfactory qualitative agreement of the calculated and the measured curves is achieved. The position of the point dipole is usually within the real tip space and its position and the magnetic strength are fit parameters.[24] In other words, the local magnetization of the tip coating is weighted by the stray field of the sample at the respective positions and subsequently added. Due to the decay of the stray field with increasing distance from the sample, the position of the effective magnetization is at a distance δz away from the apex, inside the tip. The advantage of this model is that Eq. (7) simplifies to a multiplication of a function of the field $\mathbf{H}_s$ with the monopole or dipole moment of the tip at the effective position z_{eff} (which is δz above the tip-sample distance z_0). Numerical simulations based on this approach are very fast; however, the tip parameters z_{eff} and M_{tip} are physically unreasonable. The extreme simplification of the tip magnetization has two major disadvantages: (1) the tip geometry is omitted from the simulation and (2) reliable results are only obtained in the case that the investigated sample stray field shows the same decay behavior and a similar geometry as the tip stray field.

Naturally, a quantitative tip model is more complex than the simple models discussed above. Nevertheless, the increased complexity can lead to a reliable and precise tip model. For this purpose, more useful tip parameters that directly reflect experimentally accessible properties of the tip have to be incorporated. Consequently, we modeled the tip as a cone with an opening angle γ, terminated by a spherical apex (radius r, see Fig. 4). The two geometrical tip functions were continuously merged at the point where the cone touches tangentially the sphere (see Fig. 4). The magnetic properties of the coating are defined by its thickness δ_{tip} and remanent magnetization $\mathbf{M}_{\text{tip}}^{\text{rem}}$. Furthermore, the magnetic coating is treated as a multishell structure of magnetic dipoles. All dipoles are oriented in the z direction. Within this model, the influence of the geometrical and magnetic prop-

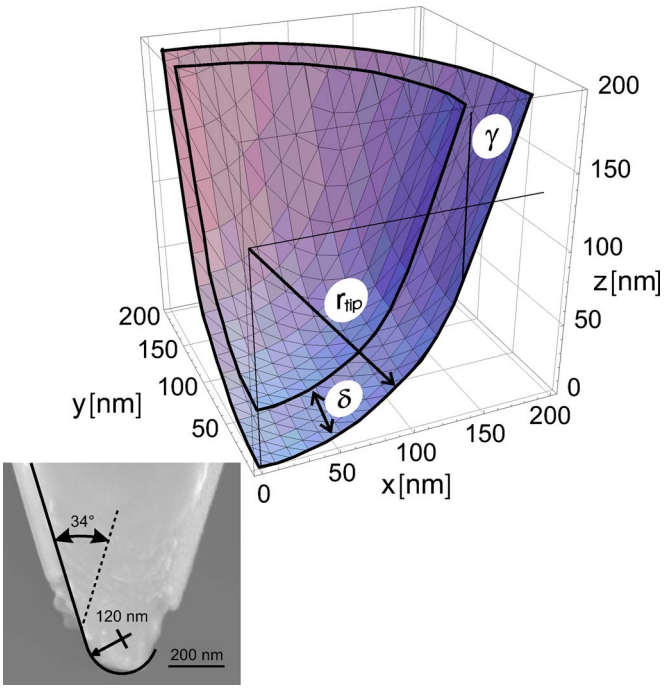

FIG. 4. Top: geometry of the modeled tip. Bottom: scanning electron micrograph of a MFM tip. The tip radius is $r_{\mathrm{tip}}=120$ nm and the cone opening angle $2\gamma=34°$. As the tip coating is partially worn of, its thickness can be determined to $\delta=20$ nm.

erties on the MFM response can be systematically studied—numerically as well as experimentally. Compared to the simple point probe approximation, a more computing-intensive treatment of Eq. (7) is necessary.

C. Model of the sample stray field

As motivated above, we model the micromagnetic structure of stripes in the thin MnAs film as an arrangement of bar magnets with a constant, but alternating magnetization **M**. In this model, the individual in-plane magnetized bar magnets are separated by out-of-plane magnetized bar magnets representing 180° Bloch walls. Recently, we derived an analytic expression of the magnetic field of a bar magnet that allows for a faster calculation of the stray field of a complex magnetization pattern by simple superposition.[33]

In detail, the simulated structure has the following dimensions: width of the ferromagnetic stripe (along the *a* axis) of 700 nm, width of the individual domain (along the *c* axis) of 190 nm, film thickness of 180 nm, saturation magnetization of 800 kA/m, and effective Bloch wall width of 30 nm. These parameters are representative for room-temperature experiments on a 180-nm-thick MnAs film on GaAs(001). Figure 5 shows a cross section (at $x=0$) of the stray field along the *a* axis of an individual domain in MnAs. The vectors show the direction of $H_{x=0,y,z}$ only. The underlying gray scale image shows the values of H_z, normalized at each respective height. It should be noted that, using the analytic expression given in Ref. 33, the second derivative of the stray field behaves well as we are only interested in the upper half-space above the sample. Furthermore, the divergences of the field at the corners of the bar magnet can be ignored, as the stray field is calculated sufficiently far away from these points.

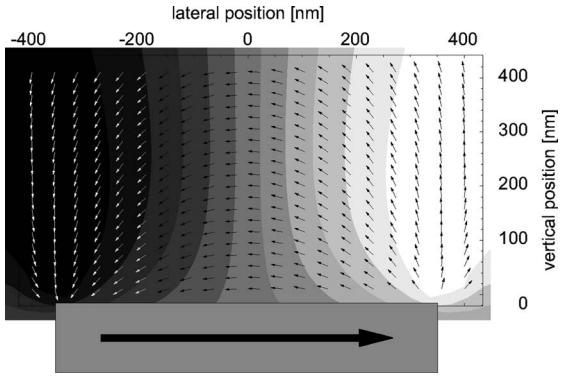

FIG. 5. Cross-sectional view of the stray field of an individual domain along the easy *a* axis. The dimensions are given in nm.

D. Simulation of the MFM response

Based on the assumption that the tip magnetization lies predominantly along the *z* axis upon magnetization along its axis prior to the MFM experiments, we restrict ourselves to the treatment of the *z* component of the magnetic field of the sample. Now, the integral in the expression for the force gradient [Eq. (7)] simplifies to a summation:

$$F_z'(\mathbf{r}) = \mu_0 \sum_{\mathrm{tip}} \left[M_{z,\mathrm{tip}}(\mathbf{r}') \cdot \frac{\partial^2}{\partial z^2} H_z(\mathbf{r}-\mathbf{r}') d^3\mathbf{r}' \right]. \tag{8}$$

The (x,y) plane is discretized introducing an equidistant step size δ_s. Then, the values $z_s(i\delta_s, j\delta_s)$ are calculated for the given tip geometry and an approximation for Eq. (6) is obtained:

$$F_z'(x,y,z) = \mu_0 \sum_{i,j} \left[M_{z,\mathrm{tip}}(x+i\delta_s, y+j\delta_s, z_s) \times \frac{\partial^2}{\partial z^2} H_z(x+i\delta_s, y+j\delta_s, z_0+z_s) \right]. \tag{9}$$

The MFM response is further calculated from Eq. (9) requiring the tip and sample input parameters as well as the tip-sample distance. The resulting force gradient leads, together with the cantilever parameters, to the MFM response. The detailed flow chart of the simulation procedure is depicted in Fig. 6.

The expenditure of time required for the calculation of the MFM response in a point above the sample depends on the rank of the involved matrices and is thus a function of the sampling grid. In case of the tip matrix, its rank depends on the density and distribution of dipoles required for a sufficient sampling of the tip. This is, in turn, not only depending on the tip geometry but also on the decay length of the sample stray field. For practical calculations, a trade-off has to be made between the precision of the simulation and the computing time. In principle, starting from a measured MFM contrast, the experimental values of tip-sample distance z_0

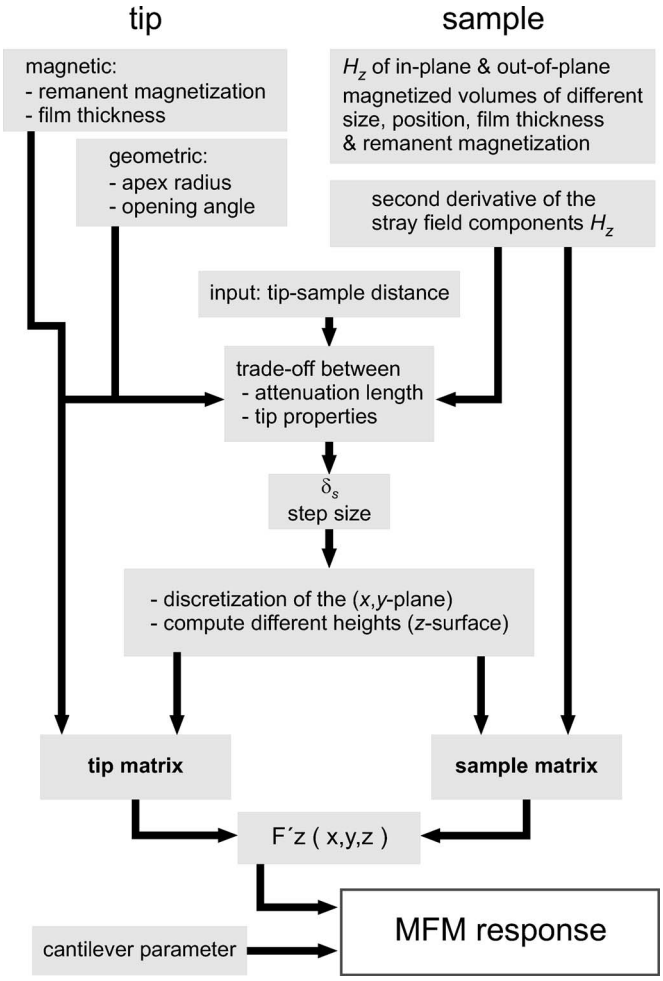

FIG. 6. Flow chart of the simulation procedure.

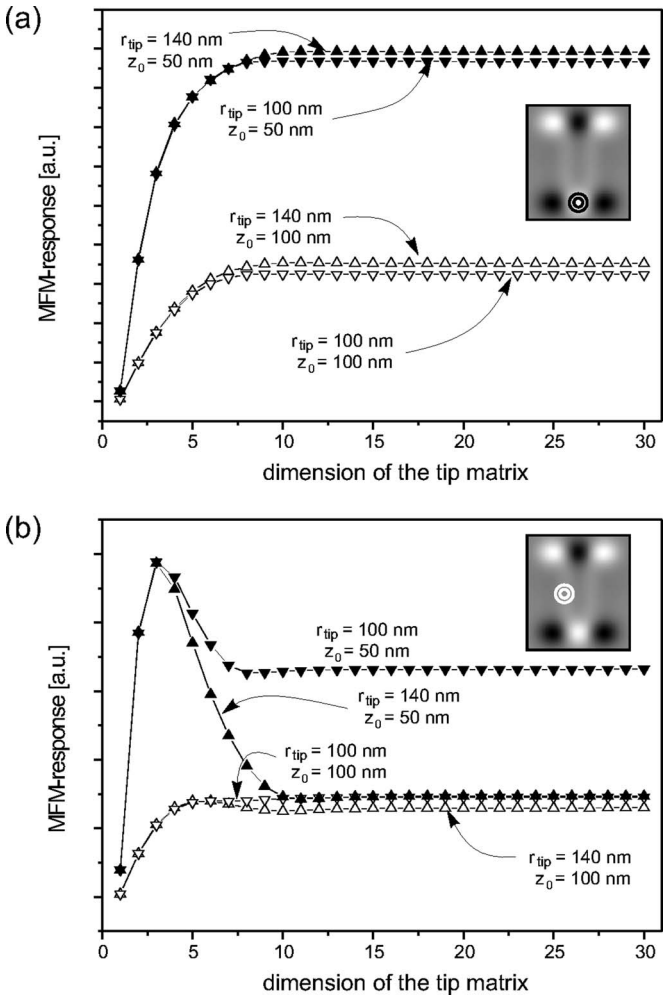

FIG. 7. Plots of the MFM response above characteristic points of the sample as indicated in the figure (see insets): (a) above the end of the in-plane bar magnet and (b) above the Bloch wall. The calculations were performed at tip-sample distances of 50 and 100 nm using tip radii of curvature of 100 and 140 nm, respectively. The cone opening angle of the tip is 10°.

and oscillation amplitude A_d can be used as fitting parameters for obtaining a good agreement between measured and calculated contrasts.

To estimate the tip dimension—and thus the rank of the tip matrix—that has to be taken into account for a correct simulation, we calculated the MFM response above characteristic points of the sample as a function of the dimension of the tip matrix. Figure 7 shows the results for two tip radii of curvature (r_{tip}=100 and 140 nm) at two tip-sample distances (z_0=50 and 100 nm). In (a), the curves obtained above the end of an in-plane magnetized bar magnet are shown. The shape of the curves is similar, however, exhibiting a stronger MFM response in case of smaller tip-sample distances. The tip geometry has no significant influence on the curves. It is found that in the case of z_0=50 nm, the tip matrix dimension n has to be larger than 10, whereas for z_0=100 nm, $n \geqslant 8$.

A different behavior is observed for the out-of-plane magnetization within a Bloch wall, modeled by a bar magnet with a width of 10 nm. For a large tip-sample distance (z_0=100 nm), the tip geometry has only a minor influence on the MFM response and $n \geqslant 10$ is sufficient for distinguishing the different tip shapes. When the tip is kept at small distances above the sample (z_0=50 nm), a dramatic influence of the tip geometry is observed due to the relative dimensions of tip and bar magnet. First, using a small tip matrix, the MFM response is overestimated. For $n>5$, the tip geometry has a large impact on the response. Whereas for a tip radius of 100 nm, n=7 is sufficient, a larger tip (r_{tip}=140 nm) requires $n \geqslant 10$. The tip geometry and tip-sample distance dependence of the MFM response can be easily understood bearing the distribution of the second derivative of the stray field in mind.[25] As a consequence of the close vicinity of areas with opposite signs of $\partial^2 H_z/\partial z^2$, the MFM response is a strong function of the sampled area. For example, in the case of a flat tip, large oppositely oriented areas ($\partial^2 H_z/\partial z^2$) contribute to the overall signal.

Figure 8 shows the simulated domain structure (a), consisting of three oppositely magnetized domains (190 nm wide, 700 nm long, 180 nm thick, saturation magnetization of 800 kA/m) embedded in nonmagnetic material. The z component of the magnetic stray field H is presented in (b) at a height of 100 nm. H_z shows a strong, smeared out contrast over the end of the in-plane domains. On the other hand, the stray field of the out-of-plane magnetization (Bloch wall) is hardly visible. For the second derivative of the magnetic stray field $\partial^2 H_z/\partial z^2$, shown in (c), a strong contrast enhancement of the out-of-plane magnetization is obvious. More-

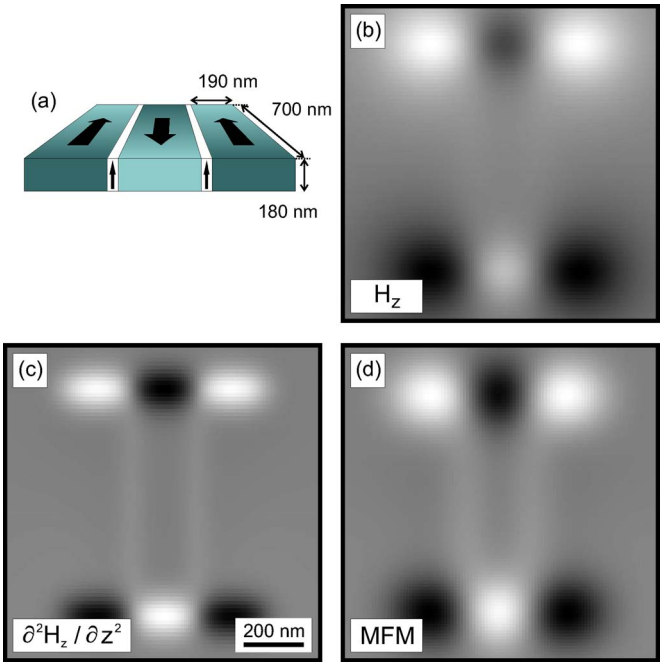

FIG. 8. (a) Model of the simulated domain structure. (b) H_z component of the stray field and (c) its second derivative at a height of 100 nm; the corresponding MFM response is shown in (d).

over, the contrast of the in-plane domains is strongly localized at the ends of the domains. It is worth noting that the $\partial^2 H_z/\partial z^2$ image is identical with the MFM response for a strongly simplified tip represented by a single dipole. The artificial introduction of the effective position of the single tip dipole causes a less-localized and strongly underestimated MFM response. In general, the method compensates the lower MFM response by an overestimation of the dipole strength. The general MFM response (d) is given by the convolution of $\partial^2 H_z/\partial z^2$ with the realistic tip model (tip radius of curvature of 100 nm, magnetic coating thickness of 40 nm, cone opening angle of 10 nm, saturation magnetization of 700 kA/m). Now, the finite size of the tip broadens the localized $\partial^2 H_z/\partial z^2$-signal. The MFM image resembles the distribution of the stray field H_z (b) with the main difference that the Bloch walls show an enhanced contrast.

Summarizing these results, an improved simulation of the MFM response in real space is presented. This way, in principle, arbitrary tip shapes and sample stray fields—provided that they can be approximated by an analytical expression—can be simulated quantitatively.

IV. MFM RESPONSE: MICROMAGNETIC SOLUTION

We now discuss a three-dimensional micromagnetic simulation of the MFM response due to the magnetic domain configuration introduced in Sec. II. The numerical simulation is performed on a micromagnetic simulator[56] assuming absolutely hard magnetization conditions of the tip and the sample, i.e., no energy minimization is performed on the simulated system and no mutual tip-sample interaction is accounted for—in contrast to the work of Scheinfein *et al.*[32] and Mansuripur.[31] However, the advantage of our approach is that arbitrary, three-dimensional sample and tip magnetization distributions can be simulated in reasonable times. For each tip position, a numerical evaluation of the second derivative of the overall micromagnetic energy, excluding the sample demagnetization, has to be performed, yielding the force gradient and thus the MFM response.

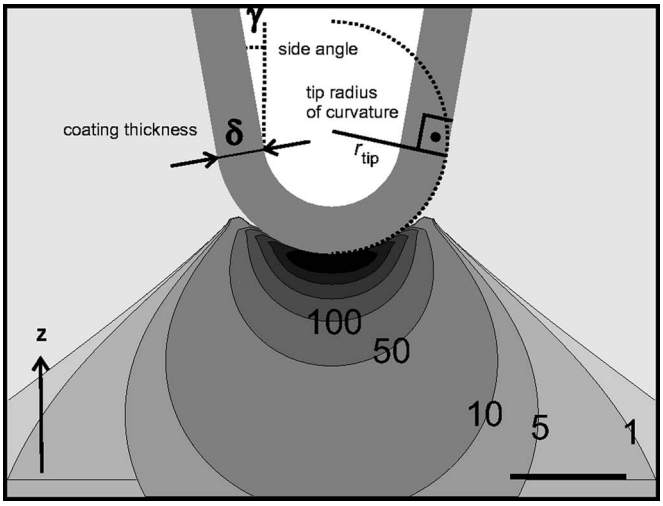

FIG. 9. Geometrical model of the tip showing the cone opening angle γ, the coating thickness δ, and the tip radius of curvature r_{tip}. Contours of the z component of the calculated tip stray field are shown for $\gamma=10°$, $\delta=40$ nm, and $r_{tip}=100$ nm. The values are given in mT in the figure. The bar on the lower right-hand side represents a length of 100 nm.

A. Description of the simulation procedure

For the micromagnetic solution, a tip of finite size is placed at a certain height z_0 above the magnetic sample, and the entire structure is discretized in all three dimensions (cell size: $\Delta x \times \Delta y \times \Delta z$). The tip is assumed to have a constant magnetization and a tip shape defined by the radius of curvature r_{tip}, the side angle γ, and a coating thickness δ [see Fig. 9]. It has to be noted that, in principle, arbitrary tip magnetizations can be included in the simulation. This also applies to magnetization distributions obtained for completely relaxed tip-sample systems using Landau-Lifshitz-Gilbert equation. In the present case, the tip is approximated by a cone with opening angle γ with a continuous transition to a spherical tip cap of radius r_{tip}. For simplicity, the magnetization is further assumed to be oriented along the z axis. We consider a finite tip height l_z yielding $n=l_z/\Delta z$ number of layers in the tip using the discretization mentioned above. Each layer consists of a ring of magnetic material. In order to achieve a reasonable discretization of the tip, the average moment of magnetization in each cell is calculated by averaging the analytical values of the eight corner points of the cell. Figure 9 shows the simulated stray field of the tip with the same parameters used for the tip in Sec. III [see Fig. 4: $r_{tip}=100$ nm, $\delta=40$ nm, $\gamma=10°$].

According to Eq. (3), the MFM response (frequency shift) is proportional to the force gradient and thus in an approximate view proportional to the second derivative of the magnetostatic energy between tip and sample with respect to the z direction: $\Delta\omega \sim F' \sim E''_{ms}$. The common five-

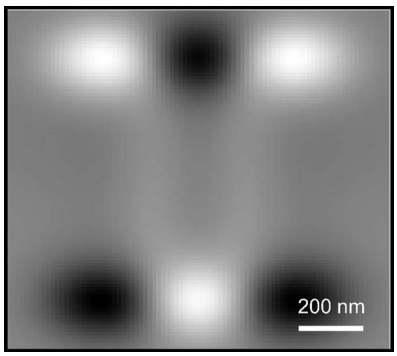

FIG. 10. Simulated MFM image of the micromagnetic domain structure [see Fig. 8(a)] based on the micromagnetic approach.

point approximation is used for obtaining the second derivative of the magnetostatic energy with respect to z by numerical differentiation:

$$E''_{\mathrm{ms}} = [-E_{\mathrm{ms}}(z_0 - 2\Delta z) + 16E_{\mathrm{ms}}(z_0 - \Delta z) - 30E_{\mathrm{ms}}(z_0) + 16E_{\mathrm{ms}}(z_0 + \Delta z) - E_{\mathrm{ms}}(z_0 + 2\Delta z)]/12(\Delta z)^2. \quad (10)$$

The complete MFM image is then obtained by raster scanning the tip across the sample in steps of Δx and Δy and calculating E''_{ms} at each scan position.

The magnetostatic energy is given by

$$E_{\mathrm{ms}} = \sum_i \mathbf{M}_{\mathrm{tip}}(\mathbf{r}_i) \cdot \mathbf{H}_s(\mathbf{r}_i), \quad (11)$$

where $\mathbf{M}_{\mathrm{tip}}(\mathbf{r}_i)$ is the magnetization of the tip and $\mathbf{H}_s(\mathbf{r}_i)$ the stray field of the sample at tip cell i. To speed up the simulation, we use the convolution theorem to calculate the stray field of the sample as follows:

$$\mathbf{H}_s(\mathbf{r}_i) = -\sum_j \underline{\underline{\mathbf{N}}}(\mathbf{r}_i - \mathbf{r}_j) \cdot \mathbf{M}_s(\mathbf{r}_j), \quad (12)$$

with $\underline{\underline{\mathbf{N}}}(\mathbf{r}_n - \mathbf{r}_j)$ the demagnetization tensor calculated once at the beginning of the simulation.[57]

B. MFM response

Figure 10 shows a grayscale image of the MFM response for the sequence of three oppositely magnetized, neighboring domains [see Fig. 8(a)]. The simulated structure is identical for both the analytical and numerical simulations. The contrast is dominated by bright and dark areas, located at the ends of the three simulated domains. At a tip-sample distance $z_0 = 100$ nm, the bright areas are centered around the borders of the geometrical dimensions of the domains (length $\times$ width $= 700 \times 190$ nm^2). Between the domains, the Bloch wall yields a much weaker contrast than the dominating contrast from the in-plane domains ($\approx 1/10$). As a consequence, a series of oppositely magnetized domains appears as a meanderlike structure in MFM experiments. The apparent width of the Bloch walls is determined by the convolution of its stray field with the tip and will be closer investigated in the following section.

As in the case of the analytical model, the influence of the tip sampling has to be carefully investigated. For this purpose, we evaluated the MFM response atop of an area of maximum contrast caused by an in-plane domain and an out-of-plane magnetization (Bloch wall), respectively. Figure 11 shows logarithmic plots of the MFM response as a function of the number of tip layers n for the in-plane domain maximum (upper curve) and the out-of-plane contrast maximum (lower curve), respectively. The step size in the z direction is 10 nm. As expected, the MFM signal is about an order of magnitude weaker above the center of a Bloch wall compared to an in-plane magnetized domain. From the curves, it is obvious that the MFM response starts to converge for n at least >10.

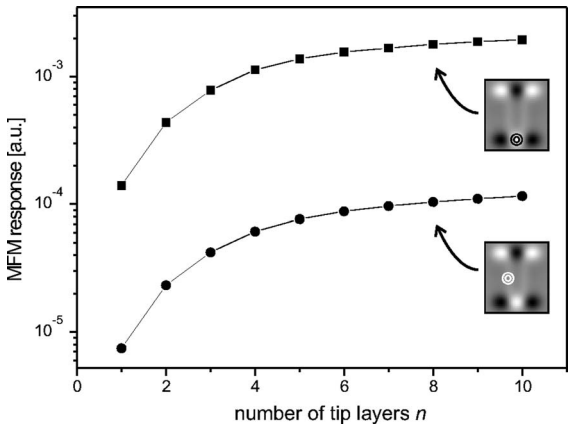

FIG. 11. Logarithmic plot of the MFM response as a function of the number of tip layers ($\Delta z = 10$ nm) above an area of maximum contrast caused by an in-plane domain (upper curve) and an out-of-plane magnetization (Bloch wall, lower curve), respectively. The positions are indicated in the respective insets. The tip-sample distance is $z_0 = 100$ nm.

C. Simulation of a 180° Bloch wall: Simplified versus realistic model

So far, we evaluated a simplified model for a 180° Bloch wall where the magnetization was assumed to be constant and normal to the surface over the effective width of the wall. Then, the interaction is attractive (repulsive) in case the tip and wall magnetizations are parallel (antiparallel). In order to estimate the applicability of the simplification, we performed MFM simulation for an ideal 180° Bloch wall. For the investigated sample, MnAs-on-GaAs(001), the wall width $w_{\mathrm{BW}} = \sqrt{A/K}$ according to the classical definition introduced by Lilley[58] was assumed to be 10 nm (A is the exchange stiffness constant and K the magnetocrystalline anisotropy constant). For the simplified Bloch wall model, the width of the bar magnet has to be $w_{\mathrm{sBW}} = \pi w_{\mathrm{BW}}$; however, as the cell size for simulation was 10 nm, we chose $w_{\mathrm{sBW}} = 30$ nm.

Figure 12 shows a comparison of the MFM response obtained for a realistic Bloch wall model (left) and the simplified Bloch wall model (right). The transition of the magnetization within the two Bloch wall models is shown above. In the middle, the images of the simulated MFM response are shown. The walls show up as either bright or dark areas, corresponding to repulsive or attractive forces, respectively. The contrast can be understood by taking a closer look at the ideal 180° Bloch wall, where the magnetization can rotate in two ways. Within the wall, the magnetization points either

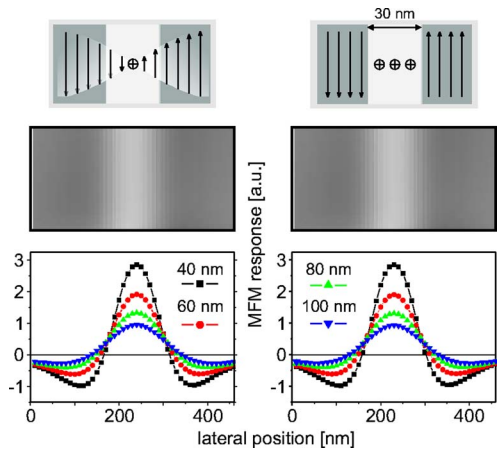

FIG. 12. Simulation of the MFM response of a realistic 180° Bloch wall (left) and the simplified model based on an out-of-plane magnetized bar magnet (right). The magnetization distribution within the domain wall wall is presented above (not to scale). The MFM response shows virtually identical images (middle) for both wall models, which is confirmed looking at the line profiles for four different tip-sample distances z_0 (below).

into (out of) the plane, giving rise to an attractive (repulsive) interaction for a tip magnetized in the z direction. The curves (Fig. 12, bottom) show the line profiles across the respective domain transitions for tip-sample distances z_0=40, 60, 80, and 100 nm. In general, the MFM signal and the contrast increase for lower tip-sample distances. The comparison of the line scans for both Bloch wall models reveals that for tip-sample distances >40 nm, there is virtually no difference between the two models, i.e., the simplified assumption of an out-of-plane magnetized bar magnet is an applicable approximation for a 180° Bloch wall.

V. DISCUSSION

For a quantitative comparison of the two simulation methods, we analyzed the three-domain structure [see Fig. 8(a)] incorporating simplified Bloch walls where the rotation of the magnetic moments points out of the sample plane. In both cases, a step size of 10 nm was used for the calculation. The simulation parameters were $M_{\mathrm{tip}}^{\mathrm{rem}}$=800 kA/m, $M_{\mathrm{sample}}^{\mathrm{rem}}$=700 kA/m, tip-sample distance z_0=100 nm, r_{tip}=100 nm, δ_{tip}=40 nm, and δ_{sample}=180 nm. Figure 13 shows line scans across an in-plane domain (labeled 1) and across the two Bloch walls 2, as indicated in the image above. For both types of contrast features, the plots agree qualitatively very well. In general, it is observed that the magnitude of the signal obtained using the numerical method is smaller than that of the signal obtained using the analytical result. This is a result of the coarse discretization of the tip that underestimates the tip magnetization in case of the numerical method with a cell dimension of 10 nm. For comparison, experimental line scans are shown as solid lines.

The advantages and limitations of the analytical method presented in Sec. III can be summarized as follows. First of all, quantitative results are obtained for the MFM response. In order to simulate real MFM problems, the van der Waals interaction can be easily implemented to account for topographically induced contrast. Moreover, arbitrary tip shapes can be approximated by a distribution of dipoles as described

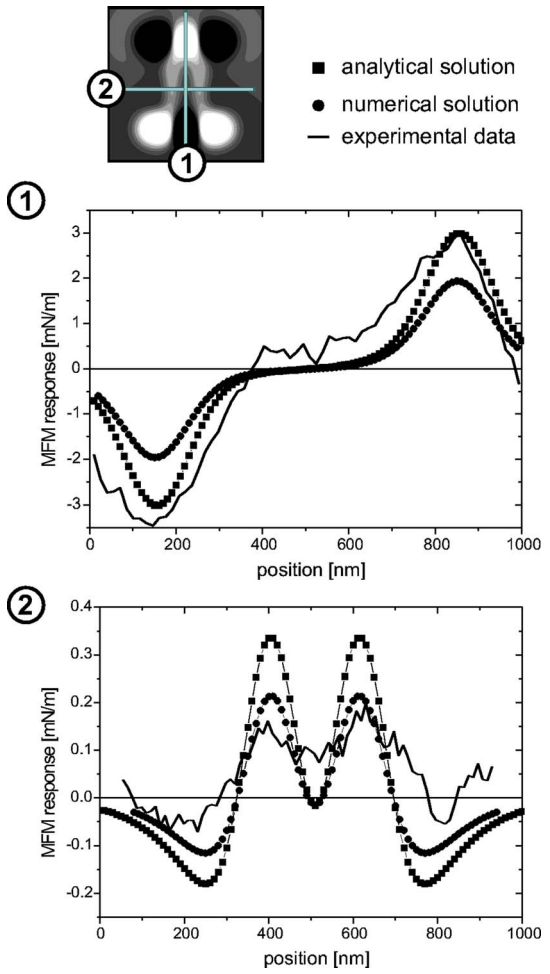

FIG. 13. Comparison of the calculated MFM response employing the analytical method (squares) and the numerical method (circles). The plots along the lines of maximum contrast across an in-plane domain are labeled 1 and the across a (simplified) Bloch wall 2. The experimental data (solid line) show a good qualitative agreement with the simulations.

above. The major limitation is the large computational effort that can be partially compensated for, using simple domain configurations where an analytical solution for the stray field is available. Moreover, only the interaction between magnetically hard tips and samples can be simulated, i.e., relaxed tip magnetizations cannot easily be obtained by iterative energy minimization.

The numerical method is characterized by the fact that arbitrary sample and tip magnetization can be the basis for the simulation. This also includes the possibility to relax the tip and the sample independently, or the entire tip-sample system in order to investigate their mutual influence.[31,32] The main advantage of the method is the short computing time (for an unrelaxed tip-sample system) which is due to the fact that the convolution theorem is employed for the calculation of the stray field. The main shortcoming is the necessary discretization of the system, especially of the tip, which leads to an underestimation of the magnetization for coarse grids. This can be somewhat compensated for by a denser sampling grid; however, due to the involved fast Fourier transform, the size of the grid is limited by the memory addressable.

Table I lists the comparison of the figures of merit for the two methods. In principle, there is a trade-off between pre-

TABLE I. Comparison of the capabilities of the analytical vs the numerical method.

	Analytical method	Numerical method
Ease of implementation	Straightforward	Time consuming
Precision	High	Depends on discretization
Computation time	Long	Short
Flexibility	Low	High
Extensibility	Difficult	Easy

cision independent of the approach, i.e., the quantitative character of the results and computing time. In terms of the ease of simulating a given experimental problem, the analytical method has a clear advantage as it allows for a straight forward translation into an initialization file. In case of the numerical method, the implementation is tedious and more time consuming. The precision of the results obtained with the two methods is, in principle, comparably high. The analytical solution delivers quantitative results, whereas for the numerical solution, the precision strongly depends on the discretization of the problem. However, the density of the simulation grid is limited by the addressable computer memory for the fast Fourier transform. The numerical method is characterized by its fast computing properties. For the equivalent problem (cell size dimension ~ 10 nm), only 600 s are necessary to obtain the MFM image compared to $>1.6\times10^5$ s in case of the analytical method. In general, the computing time scales with $N \log N$ for the numerical method compared to N^2 for the analytical method, where N is the number of grid points. Moreover, the advantages of the numerical method are the flexibility, i.e., the capability to deal with arbitrary sample and tip magnetizations, and the extensibility, i.e., the possibility to implement the mutual tip-sample disturbance.

In the future, we will perform calculations of the dynamic MFM response performing an iterative energy minimization of the tip-sample system based on the numerical method. The resulting equilibrium magnetization state of the MFM tip and the sample allows for a precise determination of their mutual influence. Especially in the case of MnAs-on-GaAs(001), not all domain configurations can be explained by micromagnetic simulations in a satisfactory way and the influence of the tip may not be neglected.

VI. CONCLUSIONS

In this paper, we have discussed the advantages and limitations of two approaches for the simulation of the MFM response in three dimensions. One approach uses an analytical solution for the stray field of a bar magnet and the MFM response is calculated as a convolution of the sample stray field with the tip magnetization (extended dipole model). The other approach breaks up the sample and the tip into cells and then calculates the energy of the magnetic tip-sample interaction. The model system, MnAs-on-GaAs(001), exhibits well-ordered ferromagnetic stripes with a simple-to-model domain structure: a sequence of alternatingly in-plane magnetized bar magnets, separated by 180° Bloch walls. Based on the simulation of this material system showing neighboring in-plane and out-of-plane magnetized areas on a submicron length scale, we compare both approaches for the simulation of the MFM contrast incorporating a realistic tip model. In general, the computational effort using the numerical method is by far smaller than for the analytical method. Moreover, the numerical approach offers greater flexibility, as in selected cases; the more time-consuming relaxation of the micromagnetic problem can be performed. On the other hand, when very small structures are to be analyzed, the precision of the analytical method is higher for a given computing time.

ACKNOWLEDGMENTS

The authors thank J. Mohanty for help with the MFM measurements and discussions. We also thank R. Koch for both helpful discussions and a critical reading of the manuscript.

[1] Y. Martin and H. K. Wickramasinghe, Appl. Phys. Lett. **50**, 1455 (1987).
[2] J. J. Sáenz *et al.*, J. Appl. Phys. **62**, 493 (1987).
[3] P. Grütter, H. J. Mamin, and D. Rugar, in *Scanning Tunneling Microscopy II: Further Applications and Related Scanning Techniques*, edited by H.-J. Güntherodt and R. Wiesendanger (Springer-Verlag, Berlin, 1992).
[4] Magnetic Microscopy of Nanostructures, edited by H. Hopster and H. P. Oepen (Springer-Verlag, Berlin, 2005).
[5] P. Grütter, A. Wadas, E. Meyer, H. Heinzelmann, H.-R. Hidber, and H.-J. Güntherodt, J. Vac. Sci. Technol. A **8**, 406 (1990).
[6] H. J. Mamin, D. Rugar, J. E. Stern, R. E. Fontana, Jr., and P. Kasiraj, Appl. Phys. Lett. **55**, 318 (1989).
[7] S. Müller-Pfeiffer, M. Schneider, and W. Zinn, Phys. Rev. B **49**, 15745 (1994).
[8] R. B. Proksch, S. Foss, and E. D. Dahlberg, IEEE Trans. Magn. **30**, 4467 (1994).
[9] B. Vellekoop, L. Abelmann, S. Porthun, and C. Lodder, J. Magn. Magn. Mater. **190**, 148 (1998).
[10] L. Abelmann *et al.*, J. Magn. Magn. Mater. **190**, 135 (1998).
[11] T. Göddenhenrich, H. Lemke, M. Mück, U. Hartmann, and C. Heiden, Appl. Phys. Lett. **57**, 2612 (1990).
[12] L. Kong and S. Y. Chou, Appl. Phys. Lett. **70**, 2043 (1997).
[13] D. G. Streblechenko, M. R. Scheinfein, M. Mankos, and K. Babcock, IEEE Trans. Magn. **32**, 4124 (1996).
[14] S. McVitie, R. P. Ferrier, J. Scott, G. S. White, and A. Gallagher, J. Appl. Phys. **89**, 3656 (2001).
[15] J. Scott, S. McVitie, R. P. Ferrier, and A. Gallagher, J. Phys. D **34**, 1326 (2001).
[16] A. Thiaville, L. Belliard, D. Majer, E. Zeldov, and J. Miltat, J. Appl. Phys. **82**, 3182 (1997).
[17] J. O. Oti, IEEE Trans. Magn. **29**, 2359 (1993).
[18] S. L. Tomlinson and A. N. Farley, J. Appl. Phys. **81**, 5029 (1997).
[19] X. Zhu and P. Grütter, MRS Bull. **29**, 457 (2004).
[20] U. Hartmann, J. Vac. Sci. Technol. A **8**, 411 (1990).
[21] E. D. Dahlberg and J.-G. Zhu, Phys. Today **48**(4), 34 (1995).
[22] U. Hartmann, Phys. Lett. A **137**, 475 (1989).
[23] F. Kaisinger, H. Starke, G. Persch, U. Hartmann, and F. Krause, Thin Solid Films **264**, 141 (1995).
[24] J. Lohau, S. Kirsch, A. Carl, G. Dumpich, and E. F. Wassermann, J. Appl. Phys. **86**, 3410 (1999).
[25] D. Rugar, H. J. Mamin, P. Guenther, S. E. Lambert, J. E. Stern, I. McFadyen, and T. Yogi, J. Appl. Phys. **68**, 1169 (1990).
[26] S. Hosaka, A. Kikukawa, and Y. Honda, Jpn. J. Appl. Phys., Part 1 **33**, 3779 (1994).
[27] D. V. Ovchinnikov and A. A. Bukharaev, Tech. Phys. **46**, 1014 (2001).
[28] H. J. Hug *et al.*, J. Appl. Phys. **83**, 5609 (1998).
[29] S. Porthun, L. Abelmann, S. J. L. Vellekoop, J. C. Lodder, and H. J. Hug, Appl. Phys. A: Mater. Sci. Process. **66**, S1185 (1998).
[30] J. M. García, A. Thiaville, J. Miltat, K. J. Kirk, J. N. Chapman, and F. Alouges, Appl. Phys. Lett. **79**, 656 (2001).
[31] M. Mansuripur, IEEE Trans. Magn. **25**, 3467 (1989).

[32]M. R. Scheinfein, J. Unguris, D. T. Pierce, and R. J. Celotta, J. Appl. Phys. **67**, 5932 (1990).
[33]R. Engel-Herbert and T. Hesjedal, J. Appl. Phys. **97**, 074504 (2005).
[34]T. E. Schäffer, M. Radmacher, and R. Proksch, J. Appl. Phys. **94**, 6525 (2003).
[35]M. Ramsteiner *et al.*, Phys. Rev. B **66**, 081304 (2002).
[36]C. Pampuch, A. K. Das, A. Ney, L. Däweritz, R. Koch, and K. H. Ploog, Phys. Rev. Lett. **91**, 147203 (2003).
[37]M. Tanaka, J. P. Harbison, M. C. Park, Y. S. Park, T. Shin, and G. M. Rothberg, J. Appl. Phys. **76**, 6278 (1994).
[38]F. Schippan, A. Trampert, L. Däweritz, and K. H. Ploog, J. Vac. Sci. Technol. B **17**, 1716 (1999).
[39]L. Däweritz, M. Kästner, T. Hesjedal, T. Plake, B. Jenichen, and K. H. Ploog, J. Cryst. Growth **251**, 297 (2003).
[40]C. Guillaud, J. Phys. Radium **12**, 223 (1951).
[41]C. P. Bean and D. S. Rodbell, Phys. Rev. **126**, 104 (1962).
[42]R. H. Wilson and J. S. Kasper, Acta Crystallogr. **17**, 95 (1964).
[43]V. M. Kaganer, B. Jenichen, F. Schippan, W. Braun, L. Däweritz, and K. H. Ploog, Phys. Rev. Lett. **85**, 341 (2000).
[44]T. Plake, M. Ramsteiner, V. M. Kaganer, B. Jenichen, M. Kästner, L. Däweritz, and K. H. Ploog, Appl. Phys. Lett. **80**, 2523 (2000).
[45]B. T. M. Willis and H. P. Rooksby, Proc. Phys. Soc. London, Sect. B **67**, 290 (1954).
[46]T. Plake, T. Hesjedal, J. Mohanty, M. Kästner, L. Däweritz, and K. H. Ploog, Appl. Phys. Lett. **82**, 2308 (2003).
[47]L. Däweritz *et al.*, J. Vac. Sci. Technol. B **23**, 1759 (2005).
[48]J. Mohanty, R. Engel-Herbert, and T. Hesjedal, Appl. Phys. A: Mater. Sci. Process. **81**, 1359 (2005).
[49]The measured film thickness was ~140 nm. Besides the discussed meanderlike domain [type (I) domain], two additional domain types are commonly observed which were discussed in detail in Ref. 33.
[50]F. J. Giessibl and H. Bielefeldt, Phys. Rev. B **61**, 9968 (2000).
[51]R. D. Gomez, A. O. Pak, A. J. Anderson, E. R. Burke, A. J. Leyendecker, and I. D. Mayergoyz, J. Appl. Phys. **83**, 6226 (1998).
[52]R. Yongsunthon, J. McCoy, and E. D. Williams, J. Vac. Sci. Technol. A **19**, 1763 (2001).
[53]C. Liu, K. Lin, R. Holmes, G. J. Mankey, H. Fujiwara, H. Jiang, and H. S. Cho, J. Appl. Phys. **91**, 8849 (2002).
[54]R. Yongsunthon, A. Stanishevsky, E. D. Williams, and P. J. Rous, Appl. Phys. Lett. **82**, 3287 (2003).
[55]Th. Kebe and A. Carl, J. Appl. Phys. **95**, 775 (2004).
[56]R. Engel-Herbert, T. Hesjedal, and D. M. Schaadt (unpublished).
[57]A. J. Newell, W. Williams, and D. J. Dunlop, J. Geophys. Res., [Solid Earth] **98**, 9551 (1993).
[58]B. A. Lilley, Philos. Mag. **41**, 792 (1950).